Research Square

Preprints are preliminary reports that have not undergone peer review.
They should not be considered conclusive, used to inform clinical practice,
or referenced by the media as validated information.

Enhanced Hydrogen Sensing Performance by Modulating Energy band of $Pd/SnO_2/WO_3$ Triple-Layer Thin Film Sensor

Yu Zhang
University of Electronic Science and Technology of China
Simin Wu
University of Electronic Science and Technology of China
Duoer Tang
University of Electronic Science and Technology of China
Yao Wang
University of Electronic Science and Technology of China
Junye Zhang
University of Electronic Science and Technology of China
Hongchuan Jiang
hcjiang@uestc.edu.cn
University of Electronic Science and Technology of China
Xiaohui Zhao
University of Electronic Science and Technology of China
Xinwu Deng
University of Electronic Science and Technology of China

Research Article

Keywords: Energy band, Heterojunction, Depletion layer, Hydrogen sensor, Low concentration limit of detection

Posted Date: May 27th, 2026

DOI: https://doi.org/10.21203/rs.3.rs-9651060/v1

License: This work is licensed under a Creative Commons Attribution 4.0 International License.
Read Full License

Additional Declarations: No competing interests reported.

Version of Record: A version of this preprint was published at Journal of Materials Science: Materials in Electronics on August 1st, 2026. See the published version at https://doi.org/10.1007/s10854-026-18099-7.

Enhanced Hydrogen Sensing Performance by Modulating Energy band of $Pd/SnO_2/WO_3$ Triple-Layer Thin Film Sensor

Yu Zhang[1], Simin Wu[2], Duoer Tang[1], Yao Wang[1], Junye Zhang[1], Hongchuan Jiang[1], Xiaohui Zhao[1], Xinwu Deng[1]

1. State Key Laboratory of Electronic Thin Films and Integrated Devices, University of Electronic Science and Technology of China, Chengdu 610054, China
2. Glasgow College, University of Electronic Science and Technology of China, Chengdu 610054, China

*Corresponding author. E-mail address: hcjiang@uestc.edu.cn (H. Jiang).

Abstract: In this work, a novel composite energy band structure was designed, and a triple-layer $Pd/SnO_2/WO_3$ thin film was deposited on anodic aluminum oxide (AAO) via magnetron sputtering to fabricate a hydrogen sensor. By constructing a heterojunction barrier and a metal–semiconductor barrier, and then by optimizing the thickness, thus extended the depletion layer at the Pd/SnO_2 interface, the sensor achieves approximately twice the resistance (Rs) of the Pd/WO_3/AAO sensor and a faster recovery process than the Pd/SnO_2/AAO sensor upon exposure to 3% hydrogen. Structural and chemical analyses confirmed successful fabrication and functionalization. The optimized $Pd/SnO_2/WO_3$/AAO sensor exhibited excellent performance with a detection limit as low as 100 ppb hydrogen at a low operating temperature of 75 °C, along with superior selectivity and stability compared to control samples.

Key words: Energy band, Heterojunction, Depletion layer, Hydrogen sensor, Low concentration limit of detection

Hydrogen has great potential as a clean and renewable energy source and is considered a promising candidate to replace fossil fuels, thereby reducing environmental pollution. [1-3]Hydrogen-based energy applications are becoming increasingly important in fields such as petrochemicals, electronics, medicine, metallurgy, and the nuclear industry. [4, 5] However, hydrogen poses significant risks due to its high diffusion coefficient, low ignition point, and colorless, odorless, and tasteless nature. It can barely be detected by human senses and tends to explode when its concentration exceeds 4% in air. [1, 6, 7] Therefore, to ensure safety during hydrogen production, transportation, storage, and utilization, it is essential to develop hydrogen sensors with high sensitivity, high selectivity, an extremely low limit of detection (LOD), fast response and recovery speeds, and excellent long-term stability and reversibility.

Over the past few decades, driven by the demand for hydrogen sensors with better sensing performance, a large number of hydrogen-sensitive materials have been extensively studied and employed. Among various types of hydrogen sensors-such as catalytic combustion, thermal conductivity, electrochemical, resistive-type, and optical fiber sensors-chemiresistive sensors based on semiconducting metal oxides (SMOs) have attracted considerable attention owing to their low cost, simple fabrication, environmental friendliness, applicability in industrial emission control, biomedical fields, and household security, as well as good compatibility with microelectronic processes for long-term operation. [8]

However, single-SMO gas sensors suffer from high operating temperature, high power consumption, and poor selectivity, which severely limit their practical application. [9-12] Therefore, modulating the space charge layer is regarded as an important strategy to improve sensing performance [13-15], for instance, by introducing heterojunctions. [16-21]

In our previous work [22], a Pd/WO_{3-x}/AAO hydrogen sensor was prepared. The high concentration of oxygen vacancies in tungsten oxide (WO_3) thin films and the large surface area of the AAO substrate were exploited to enhance hydrogen sensing performance.[13, 23] The optimized Pd/WO_{3-x}/AAO sensor exhibited a significant response to hydrogen at a concentration as low as 100 ppb. To further enhance the hydrogen sensing performance, novel SMO structures are employed in this work to extend the width of the depletion layer at the Pd/SnO_2 interface.

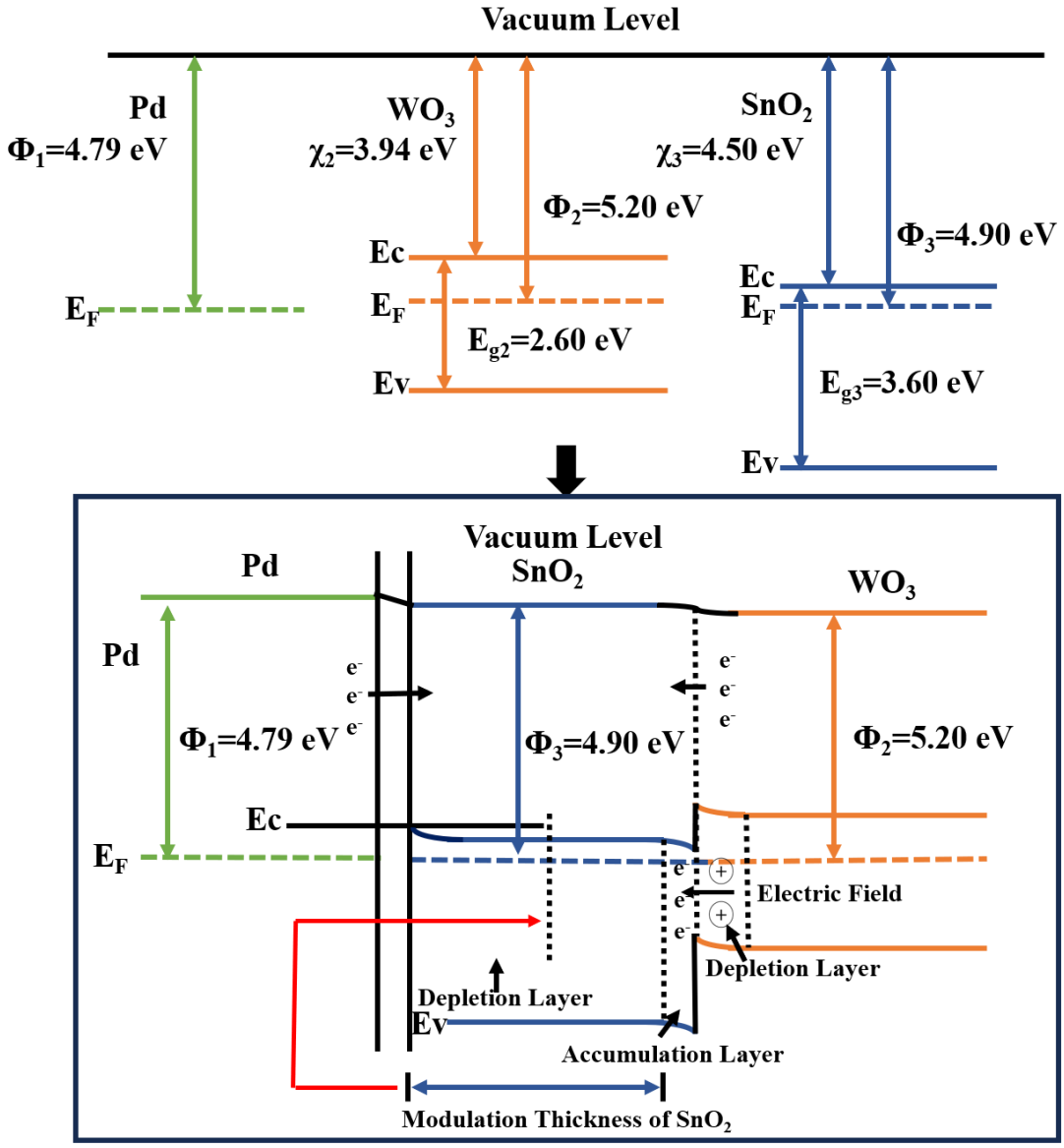


Fig. 1 The energy band of the triple-layer Pd/SnO_2/WO_3 thin film

Based on our previous work, a tin oxide (SnO_2) thin film was deposited on a WO3 film to form an n–n heterojunction. Upon formation of the SnO_2/WO_3 heterojunction, electrons transfer from WO_3 to SnO_2, which accelerates O_2 adsorption [16, 24, 25] and simultaneously extends the electron depletion layer at the Pd/SnO_2 interface[26]. As these transferred electrons are consumed by adsorbed oxygen, the heterojunction functions as an electronic valve, allowing electrons to flow continuously from the WO_3, thereby increasing the response speed and further enhancing the response magnitude. Tuning the SnO_2 thickness is crucial for the designed structure. When the SnO_2 film is too thin, its thickness becomes comparable to the width of the surface electron depletion layer. The strong coupling between the Pd/SnO_2 and SnO_2/WO_3 interfaces drives the entire SnO_2

film into a fully depleted state, causing the energy bands to bend sharply upward along the thickness direction. This enhances the surface sensitivity to hydrogen and oxygen adsorption/desorption but may induce quantum tunneling effects, thereby increasing carrier recombination and lowering the response. As the SnO_2 thickness gradually increases, the surface depletion layer is confined to the near-surface region, and a flat-band region forms inside the film, providing more conduction channels. The Pd/SnO_2 and SnO_2/WO_3 interfaces are then coupled through these conduction channels, accelerating the chemisorption/desorption of hydrogen and oxygen. Under these conditions, the conduction channel becomes a critical factor influencing gas-sensing performance, making the sensor's hydrogen sensitivity highly dependent on the SnO_2 thickness. [26] When the SnO_2 thickness becomes excessively large, the flat-band region is overly extended, bulk electron transport dominates, and the surface sensitivity to hydrogen and oxygen adsorption/desorption declines, resulting in a deterioration of the sensing performance.

2. Experimental Section

2.1 Material and sensors fabrication

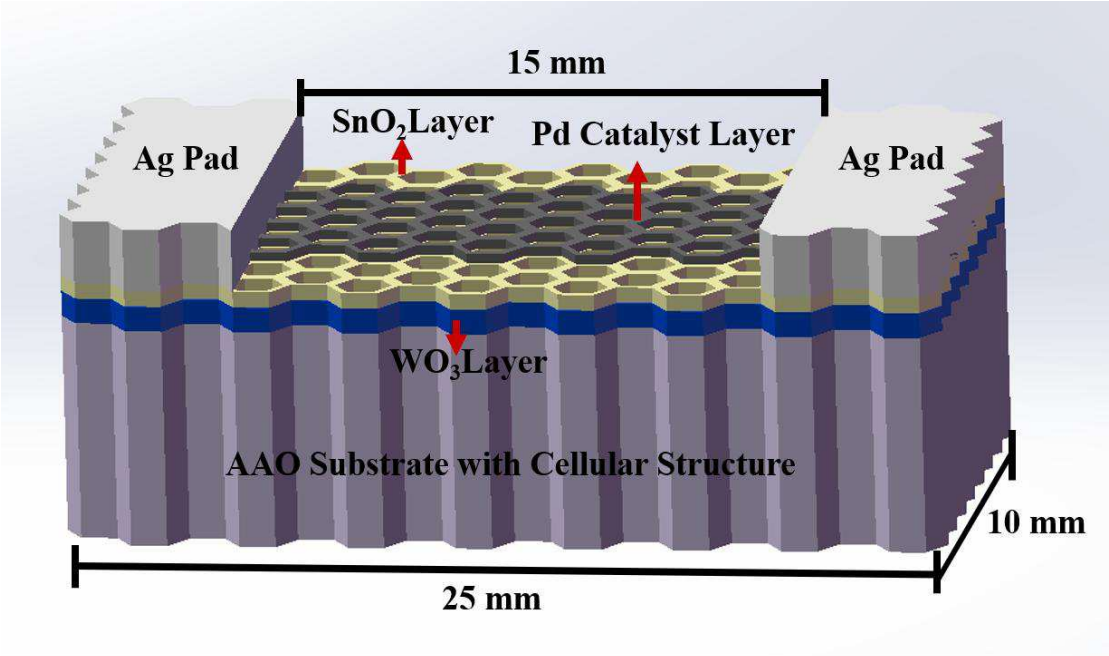


Fig. 2 Schematic of prepared hydrogen sensor

The design of the $Pd/SnO_2/WO_3$/AAO hydrogen sensor is illustrated in Fig. 2. AAO substrates with dimensions of 25 mm × 10 mm × 0.5 mm were used. The WO_3 and SnO_2 thin films served as the

hydrogen sensing layer, forming a heterojunction structure. The WO_3 film thickness was fixed at 100 nm, while SnO_2 films with varying thicknesses were deposited onto the WO_3 surface. A 5-nm-thick Pd film was then deposited onto the SnO_2 layer as a catalyst. Both ends of the rectangular substrate were coated with conductive silver paste to form electrodes.

The AAO substrates were cleaned sequentially with acetone, alcohol, and deionized water for 10 min each, and then dried in an oven at 80 °C. Subsequently, a 100 nm WO_3 thin film was deposited onto the surface of the substrates by reactive magnetron sputtering with argon and oxygen flow rates of 30 sccm and 6 sccm, respectively. The background pressure and sputtering pressure were 8×10^{-4} Pa and 0.3 Pa, respectively, and the sputtering power was 60 W. Then, SnO_2 films of varying thickness were deposited onto the WO_3 surface by reactive magnetron sputtering at a rate of ~8 nm/min, with argon and oxygen flow rates of 40 sccm and 8 sccm, respectively. The background pressure was 8×10^{-4} Pa, the sputtering pressure was 0.4 Pa, and the sputtering power was 60 W; the SnO_2 thickness was controlled by deposition time to be 1, 4, 7 and11 min respectively. After annealing at 350 °C, a 5-nm-thick Pd film was deposited by direct current (DC) magnetron sputtering over a width of 4 mm, defined by a metal mask. The background pressure, sputtering pressure, and sputtering power used for Pd deposition were identical to those employed during WO_3 deposition. Finally, conductive silver paste was applied to the surface of the AAO substrates to a thickness of 40 μm.

2.2 Material characterization

The crystalline structure was verified by X-ray diffraction radiation (XRD, PANalytical PW3040/60, Netherlands) with CuKα. The morphology of Pd/SnO_2/WO_3/AAO hydrogen sensors' surface and cross-section, and element distribution were characterized via field emission scanning electron microscopy (FE-SEM, Gemini 360, Germany) coupled with energy dispersive X-ray spectroscopy (EDS). X-ray

photoelectron spectroscope (XPS, FEI Tecnai G2 F20 S-Twin TMP, US) was utilized for detecting the chemical states, chemical bonding and work function of the surface of SnO_2 and WO_3 thin films.

2.3 Gas sensing measurement

The gas sensing measurement methods are detailed in our previous study.[2, 22] The sensors were kept in a gas chamber where the temperature could be precisely controlled and connected with a multimeter by 4 probs which were firmly pressed onto the Ag electrodes. Highly purged N_2, O_2, and N_2-H_2 w were thoroughly mixed by a gas mixer with the gas flow rates controlled by mass flowmeters to get mixed gas with different hydrogen concentration. The total gas flow rate was maintained at 100 sccm, while the gas flow rate of O_2 was kept at 21 sccm to simulate air atmosphere. The Schematic of the hydrogen measuring system is shown in Fig. 3.

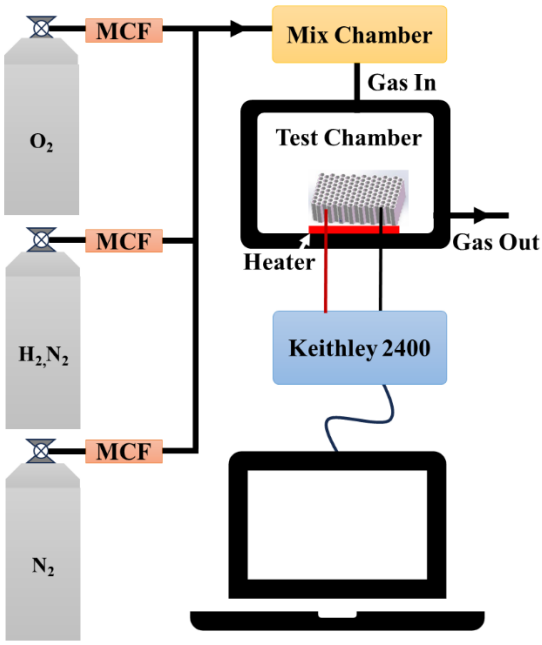


Fig. 3 Schematic of the hydrogen measuring system

The sensor response (Rs) is calculated from the relation (1):

$$Rs\ (\%)=\frac{R_g-R_a}{R_a}\times 100\ (\%) \qquad (1)$$

Where Ra and Rg are the stabilized resistances of the sensor in synthetic air and test gas with specific hydrogen concentrations, respectively. The response and recovery times (t_{rs90} and t_{rec90}) of the sensor were recorded when the resistance variation reaches 90% of the saturation value.

3. Results and discussion

The SnO_2/WO_3 thin films were deposited on silica glass substrates, the image of prepared thin films is shown in Fig. S1, and the thicknesses of the films prepared with different SnO_2 deposition times were measured using a step profiler. The results are presented in Fig. S2. The measurements showed that the WO_3 layer was approximately 100 nm thick for all samples, while the SnO_2 films deposited for 1, 4, 7, and 11 min had thicknesses of about 8, 32, 56, and 88 nm, respectively.

The XRD patterns of the WO_3, SnO_2/WO_3, and $Pd/SnO_2/WO_3$ thin films are presented in Fig. 4. It can be clearly seen that both the WO_3 and SnO_2/WO_3 films exhibit quite broad peaks, indicating that the tin oxide and tungsten oxide are in an amorphous form. This amorphization results from the fact that even minute concentrations of oxygen vacancies can significantly hinder film crystallization. [22, 27] Additionally, two peaks observed at $2\theta = 40.1°$ and 46.6° correspond to the characteristic (111) and (200) reflections of Pd, respectively, consistent with PDF#46-1043, which demonstrates that Pd was successfully loaded onto the surface of the semiconducting metal oxides.

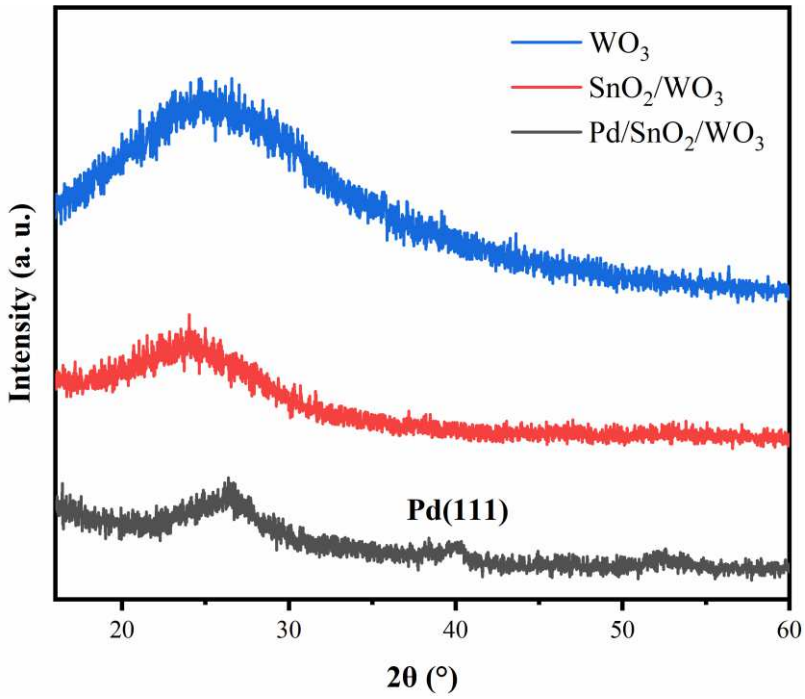


Fig. 4 XRD patterns of WO_3, SnO_2/WO_3 and $Pd/SnO_2/WO_3$ thin films.

To investigate the chemical states and elemental composition of the prepared thin films, X-ray photoelectron spectroscopy (XPS) was performed before and after Pd deposition. Adventitious carbon from atmospheric species was accounted for by calibrating all spectra to the C 1s peak at 284.6 eV. Fig. 5(a) displays the W 4f spectra of the SnO_2/WO_3/AAO samples with varying SnO_2 thicknesses. The peaks at approximately 35.6 eV and 37.7 eV correspond to W $4f_{7/2}$ and W $4f_{5/2}$ of W^{6+}, respectively.[25, 28] It can be clearly seen that the intensity of the W peaks gradually decreases with increasing SnO_2 thickness. Fig. 5(b) shows the high-resolution Sn 3d spectra of the same samples. Two distinct peaks at binding energies of 495.58 eV (Sn $3d_{3/2}$) and 487.28 eV (Sn $3d_{5/2}$) are observed and assigned to SnO_2; there is hardly any noticeable difference among the Sn 3d spectra of these samples .[16]

The high-resolution Pd 3d spectrum of the $Pd/SnO_2/WO_3$/AAO sample is shown in Fig. 6(a) and can be fitted into four peaks. The intense peaks centered at 335.1 eV and 340.5 eV are consistent with metallic Pd $3d_{5/2}$ and Pd $3d_{3/2}$, respectively, while the weaker peaks at 337.4 eV and 342.5 eV are attributed to PdO.[29] This indicates that the Pd nanoparticles on the SnO_2 surface are partially oxidized.

As shown in Fig. 6(b), the core-level Sn 3d spectra of $SnO_2/WO_3/AAO$ and $Pd/SnO_2/WO_3/AAO$ are nearly identical before and after Pd deposition. The observed presence of Pd^{2+} (evident from the Pd 3d spectrum) is attributed to electron transfer from surface Pd atoms to chemisorbed oxygen.[30] Fig. 6(c) presents the O 1s spectra of the two samples. The peak at around 530.5 eV corresponds to lattice oxygen (O_{lat}) in the oxides, whereas the peak at 532.1 eV is ascribed to surface-adsorbed oxygen species (O_{aos}) that can interact with hydrogen [16], potentially leading to reduction and water formation. After Pd deposition, the O_{aos} peak exhibits a higher intensity than that of the undecorated sample, suggesting that the Pd-decorated sample possesses a greater oxygen adsorption capacity.

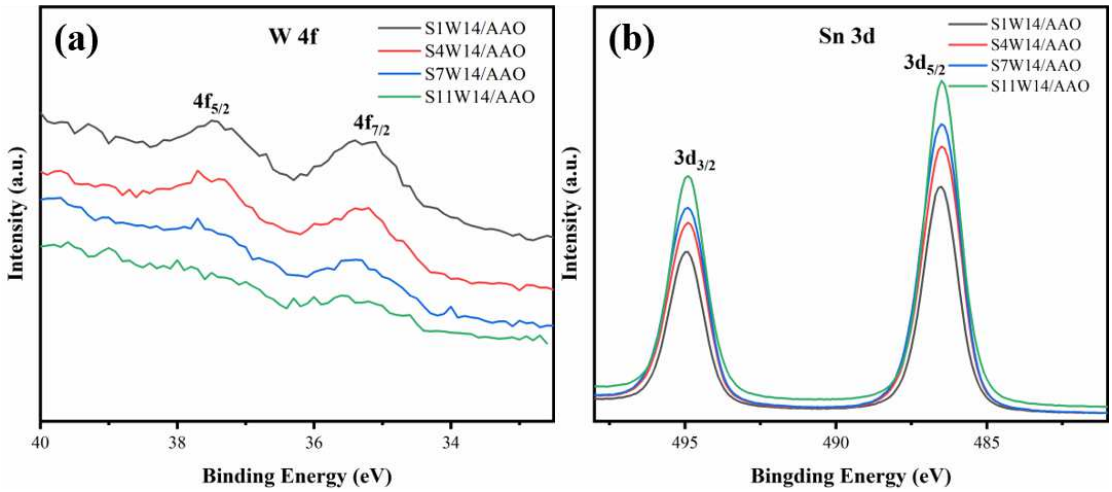


Fig. 5 XPS spectra of in W 4f and Sn 3d of the samples with different SnO_2 thin film thickness before depositing Pd, (a) W 4f, (b) Sn 3d.

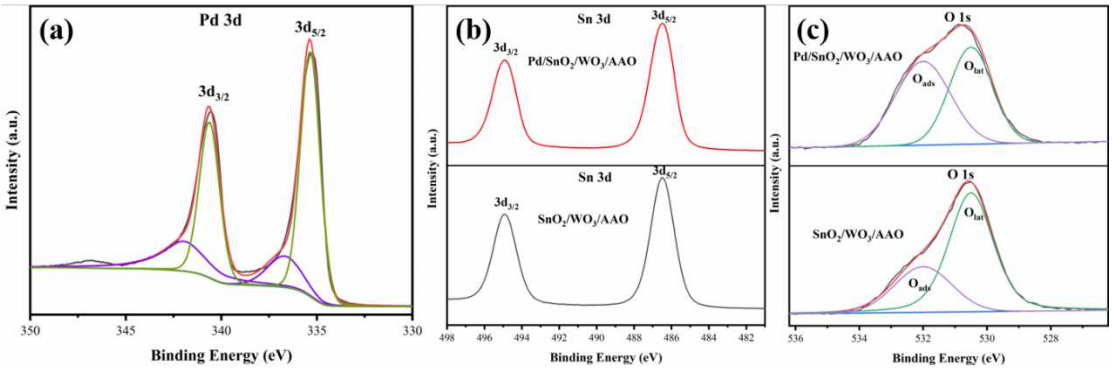


Fig. 6 XPS spectra of in Pd 3d, Sn 3d and O 1s of the samples before and after depositing Pd, (a) W 4f, (b) Sn 3d, (c)O 1s.

The microstructure of the Pd/SnO_2/WO_3/AAO hydrogen sensor is shown in Fig. 7(a). The cellular AAO framework, which features an average pore size of 250 nm, provides a large specific surface area for the growth of hydrogen-sensitive materials. Compared with planar silicon or ceramic substrates, this structure significantly increases the number of active sites available for interaction with H_2.[31] As can be seen in Fig. 7(b) at 200 000× magnification, the AAO framework is completely covered by the Pd/SnO_2/WO_3 thin films. Cross-sectional morphology images of Pd/SnO_2(56 nm)/WO_3, prepared by FIB, are displayed at 25 000× and 50 000× magnification in Figs. 7(c) and 7(d), respectively. These images further reveal that the Pd/SnO_2/WO_3 films not only coat the surface of the AAO framework but also penetrate into the pores. The film thickness is approximately 170 nm which is consistent with the stylus profilometer results, and the penetration depth into the pores is about 440 nm. The surface and cross-sectional elemental distributions of the fabricated Pd/SnO_2/WO_3 films on the AAO substrate are presented in Fig. 8. As shown in Figs. 8(b) and 8(c), the Pd, Sn, and W elements are uniformly distributed over the grid-like surface of the AAO substrate. Figures 8(e) and 8(f) display the elemental distribution across the substrate cross-section, confirming that Pd, Sn, and W atoms are predominantly located on the pore walls of the AAO substrate.

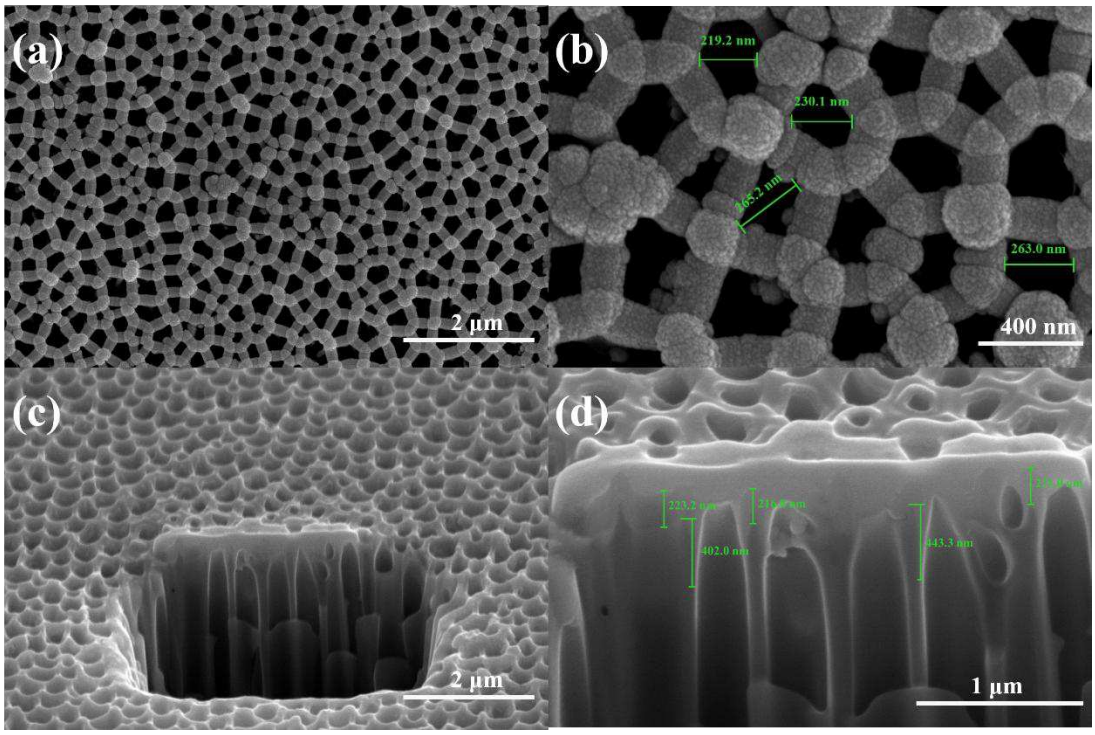


Fig. 7 SEM images of Pd/SnO_2(56 nm)/WO_3/AAO sample. (a, b) surface images, (c, d) cross-section images

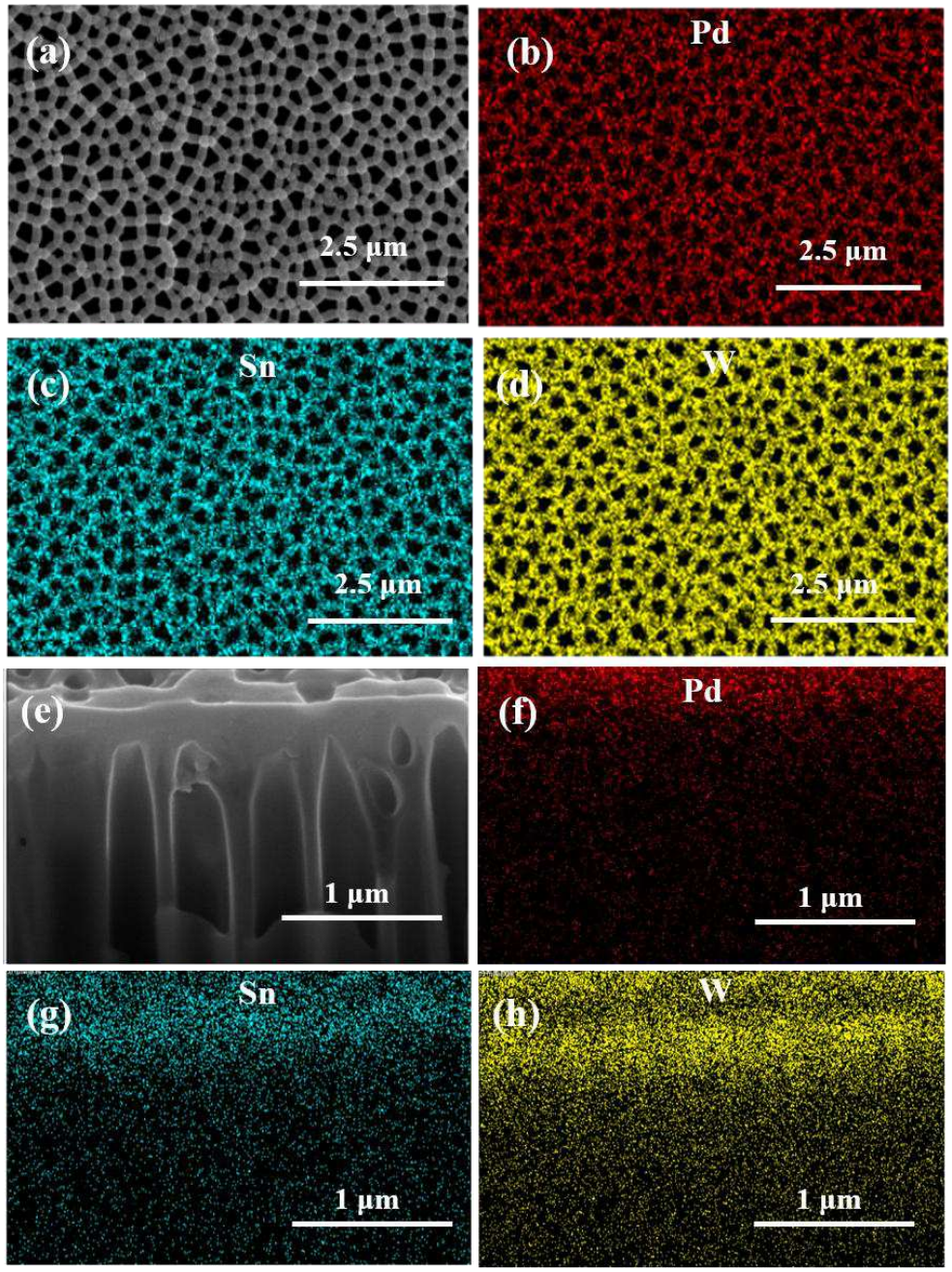


Fig. 8 Surface elements mapping and cross-section elements distribution of Pd/SnO_2(56 nm)/WO_3/AAO sample. (a) surface SEM image of capture part of Pd/SnO_2(56 nm)/WO_3/AAO sample, surface EDX element mapping for (b) Pd, (c) Sn and (d) W. (e) SEM image of capture part on the cross-section of Pd/SnO_2(56 nm)/WO_3/AAO sample, cross-section EDX element mapping for (f) Pd, (g) Sn and (h) W.

For the $Pd/SnO_2/WO_3/AAO$ hydrogen sensors, the optimal operating temperature was first determined to facilitate subsequent experiments, and the results for sensors with varying SnO_2 thicknesses are presented in Fig. 9. As the operating temperature increased, the response of all samples rose owing to the increase in temperature leads to an enhancement in the concentration of conduction band carriers.，which result in extension of the depletion layer [26], once the operating temperature reached saturation at 100 °C, a pronounced zero drift was observed in all $Pd/SnO_2/WO_3/AAO$ sensors, but not in the $Pd/WO_3/AAO$ and $Pd/SnO_2/AAO$ sensors; moreover, this zero drift weakened as the SnO_2 thickness increased. This phenomenon can be explained by the temperature-induced expansion of the depletion layer at the Pd/SnO_2 interface, which intensifies the synergistic effect between the $Pd/SnO_2/AAO$ and SnO_2/WO_3 interfaces, leading to a reduction in conduction channels. Overall, most of these sensors exhibited relatively high and stable response values along with short response and recovery times at 75 °C, and therefore 75 °C was chosen as the operating temperature for subsequent measurements.

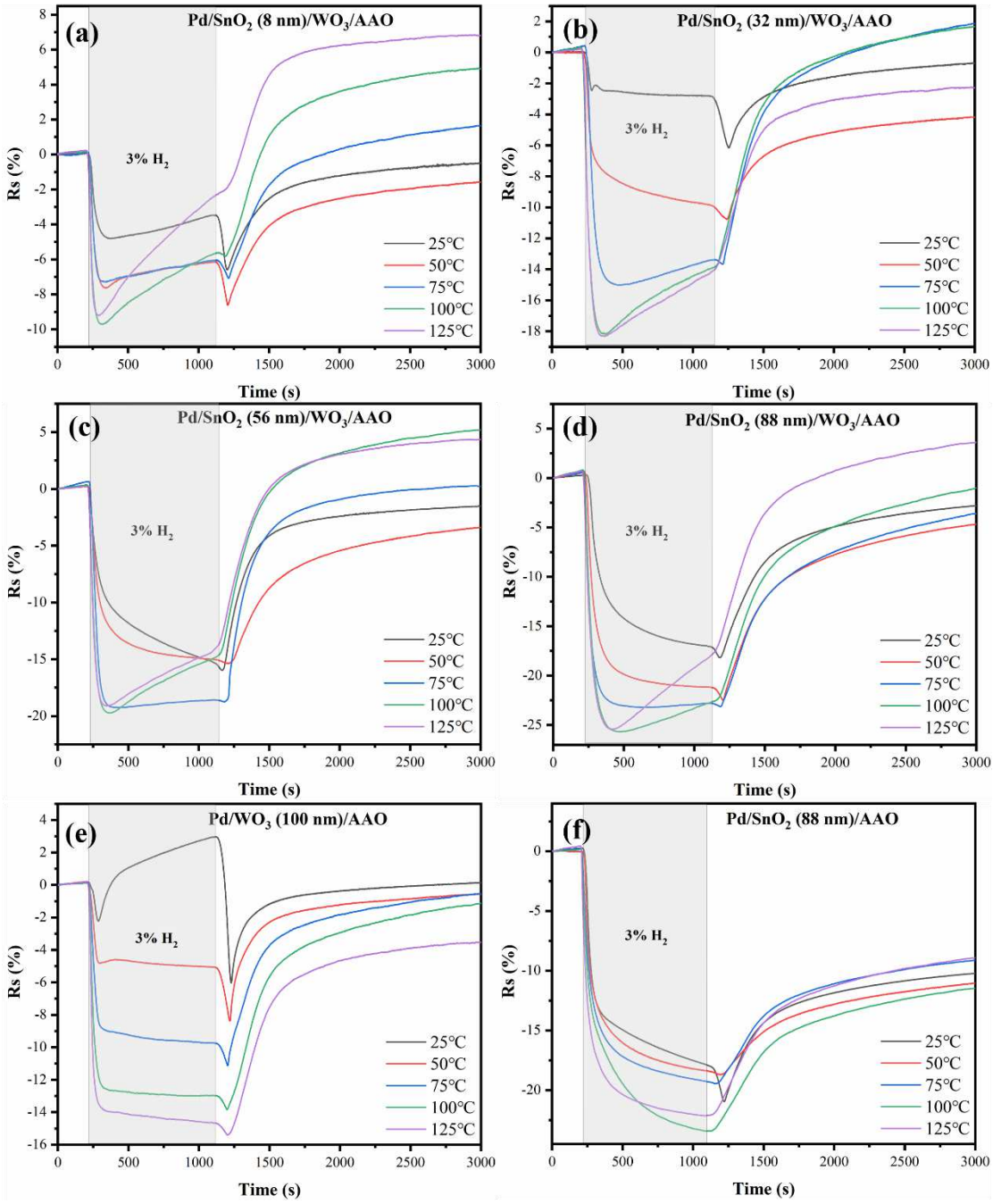


Fig. 9 Real-time resistance responses for $Pd/SnO_2/WO_3/AAO$ and $Pd/WO_3/AAO$, $Pd/SnO_2/AAO$ hydrogen sensors at varying operating temperature to 3% hydrogen in mixed gas. (a) Pd/SnO_2(8 nm)/WO_3/AAO, (b) Pd/SnO_2(32 nm)/WO_3/AAO, (c) Pd/SnO_2(56 nm)/WO_3/AAO, (d) Pd/SnO_2(88 nm)/WO_3/AAO, (e)Pd/WO_3/AAO, (f)Pd/SnO_2/AAO

Fig. 10 presents the real-time response changes of the $Pd/WO_3/AAO$, $Pd/SnO_2/AAO$, and $Pd/SnO_2/WO_3/AAO$ hydrogen sensors with different SnO_2 layer thicknesses upon exposure to 3% H_2 in

mixed gas at 75 °C. As the thickness of SnO_2 increased, the response of the Pd/SnO_2/WO_3/AAO sensors also increased within the SnO_2 thickness range of 8 nm to 88 nm. Meanwhile, the recovery time decreased while the response time increased slightly. However, although the Pd/SnO_2(88 nm)/WO_3/AAO sensor exhibited the highest response (Rs=23.21%), its recovery time was significantly longer than that of the other sensors (t_{rec90} > 2000 s). In contrast, the Pd/SnO_2(56 nm)/WO_3/AAO sensor showed the best overall performance, with a response of 19.25%, a response time (t_{rs90}) of 95 s, and a recovery time (t_{rec90}) of 590 s.

As the thickness of SnO_2 increases, the response of Pd/SnO_2/WO_3/AAO sensors increases due to the thickness of SnO_2 of prepared samples are approximate twice of the Debye length, thus, the thickness of SnO_2 determines the quantity of conduction channel which considerably effects the response value of sensor [26, 32] Except the Pd/SnO_2(8 nm)/WO_3/AAO shows lower response than Pd/WO_3/AAO sample which could attribute to the over-thin SnO_2 layer limits the quantity of conduction channel, other samples all exhibited higher response than Pd/SnO_2/AAO and Pd/WO_3/AAO sensors result from their extended depletion layers at the Pd/SnO_2 interface. The overly thick SnO_2 film weakened the interface synergy between Pd/SnO_2 and SnO_2/WO_3, causing its response performance to be more similar to that of SnO_2 itself. (the insufficient oxygen adsorption capacity prevented it from returning to the initial zero point)

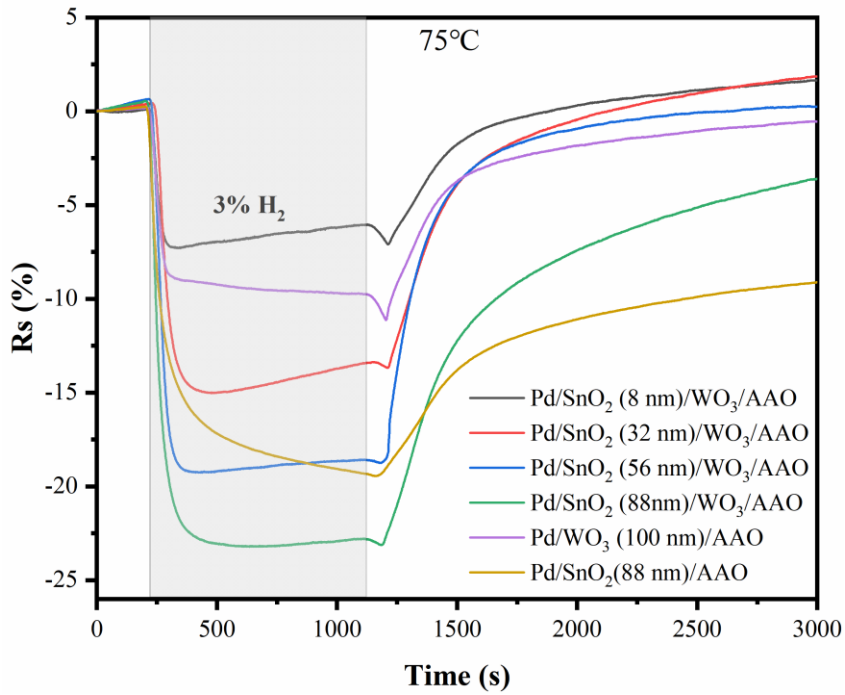


Fig. 10 Real-time responses at 75°C for Pd/SnO_2/WO_3/AAO with different SnO_2 thickness, Pd/SnO_2/AAO and Pd/WO_3/AAO sensors

The real-time resistance variations of the Pd/SnO_2/WO_3/AAO sensors with different SnO_2 thicknesses upon exposure to H_2 concentrations below 50 ppm were further investigated and are presented in Fig. 10. A resistance change could be observed for all sensors when the hydrogen concentration was increased from 0 to 1 ppm. Notably, the Pd/SnO_2(56 nm)/WO_3/AAO and Pd/SnO_2(88 nm)/WO_3/AAO samples exhibited obvious resistance changes as the concentration rose from 0 to 100 ppb, whereas the resistance changes of Pd/SnO_2(8 nm)/WO_3/AAO and Pd/SnO_2(32 nm)/WO_3/AAO under the same condition were nearly indistinguishable from the electronic noise. Calculated using Formula (1), the Rs values of the prepared samples with different SnO_2 thicknesses at low hydrogen concentrations were consistent with those measured at 3% hydrogen. Although the Pd/SnO_2(88 nm)/WO_3/AAO sensor showed a slightly higher Rs than the Pd/SnO_2(56 nm)/WO_3/AAO sensor, it also exhibited a larger zero drift. This may be attributed to the thicker depletion layer in Pd/SnO_2(56 nm)/WO_3/AAO, which induces greater electron relaxation and consequently leads to a more pronounced

zero drift. In addition, no significant difference in response time or recovery time was observed among the sensors with varying SnO_2 thicknesses, which can be explained that in a low-concentration hydrogen environment, the controlling step of the response process is the transportation of hydrogen to the surface of the sensitive material.

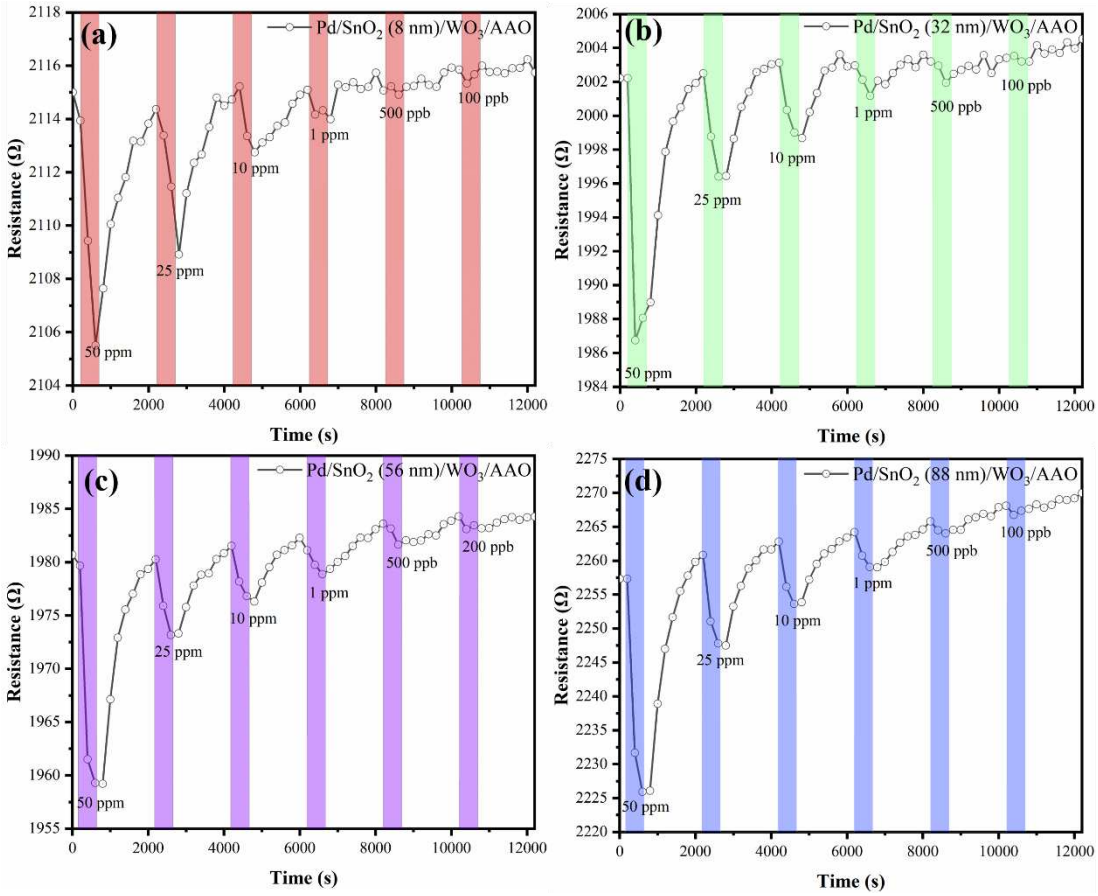


Fig. 11 Real-time resistance responses at 100℃ for H_2 with low concentration of (a) Pd/SnO_2(8 nm)/WO_3/AAO, (b) Pd/SnO_2(32 nm)/WO_3/AAO, (c) Pd/SnO_2(56 nm)/WO_3/AAO, (e) Pd/SnO_2(88 nm)/WO_3/AAO.

Fig. 12 presents the real-time resistance variation of the Pd/SnO_2(56 nm)/WO_3/AAO hydrogen sensor at 75 °C upon exposure to hydrogen concentrations ranging from 100 ppb to 1% in a mixed gas. Evidently, the sensor can effectively monitor a wide range of hydrogen concentrations. As the hydrogen concentration decreases, the sensor response decreases monotonically. Notably, a discernible resistance

change can still be observed when the hydrogen concentration increases from 0 to 500 ppb, even when the hydrogen concentration drops to as low as 100 ppb, the sensor still shows a resistance change. However, the signal stability appears to limit the ability to distinguish between 100 ppb and 500 ppb. Although this may reduce quantitative resolution, the device could still be suitable for qualitative, threshold-based detection applications at hydrogen concentrations below 500 ppb.

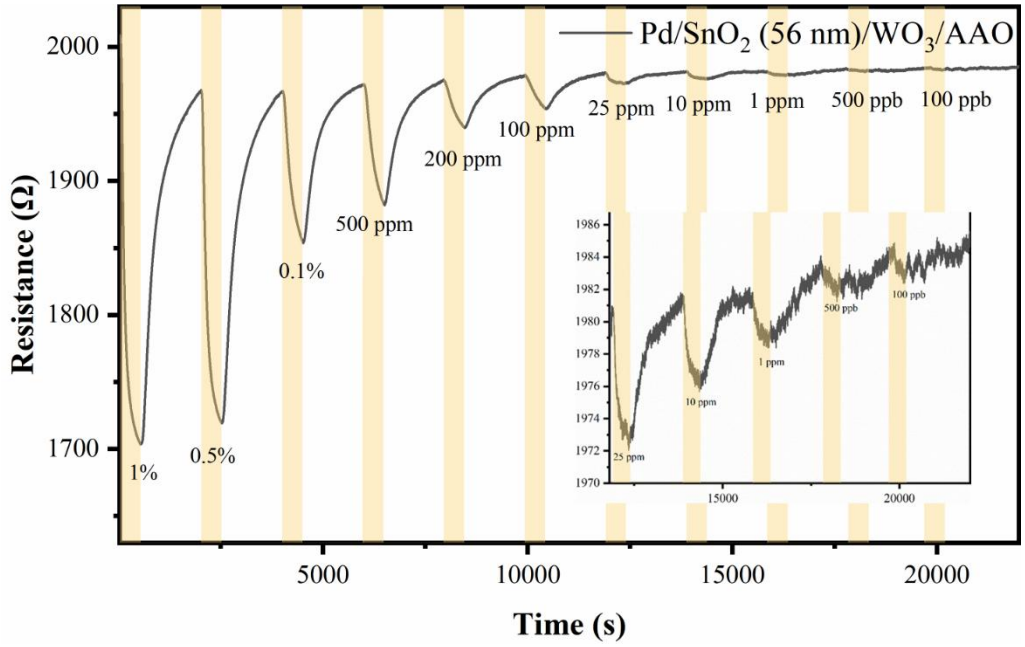


Fig. 12 Real-time resistance variation at 100℃ of Pd/SnO_2(56 nm)/WO_3/AAO sensor for various H_2 concentrations from 1% to 100 ppb (insert figure present the enlarged part of H_2 concentrations from 25 ppm to 100 ppb).

The Pd/SnO_2(56 nm)/WO_3/AAO sensor exhibits an outstanding selectivity for hydrogen. The response of Pd/SnO_2(56 nm)/WO_3/AAO to various gases with the same concentration of 1% at 75 ℃ is exhibited in Fig. 13(a). It is evidently that the response to carbon monoxide, carbon dioxide, ammonia, and methane is much lower than the 1% of hydrogen. This favourable selectivity is largely attributed to of Pd film, which remarkably decreases the activation energy for hydrogen's chemical adsorption, resulting in the low operational temperature of 75 °C and selectively limiting electron transfer between

semiconducting oxides and gases, primarily hydrogen. [33, 34] In addition, the cycling stability for Pd/SnO_2(56 nm)/WO_3/AAO to 1 % H_2 has been tested at 75 ℃ shown in Fig.13(b). After 15 cycles, the value of resistance change remains remarkably consistent, underscoring the high reproducibility of Pd/SnO_2(56 nm)/WO_3/AAO hydrogen sensor. However, a slight upward trend in resistance and decreasing trend in the value of resistance change is noticeable over time, which may owe to the relaxation processes of electrons. Subsequent work will require more finely tuned adjustment of the SnO_2 thickness and annealing treatment (including atmosphere and temperature) to further reduce the baseline drift.

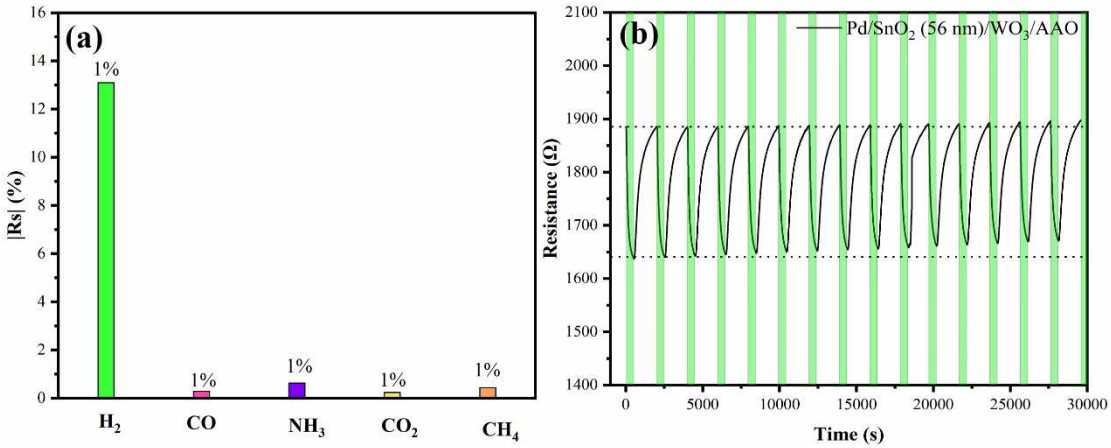


Fig. 13 (a) Selectivity of the Pd/SnO_2(56 nm)/WO_3/AAO sensor to different kinds of gases with the concentration of 1% at 75℃. (b) The cycling stability of Pd/SnO_2(56 nm)/WO_3/AAO sensor for 3% H_2 at 75℃.

Conclusion

The Pd/SnO_2/WO_3/AAO triple-layer thin film hydrogen sensor with a novel energy band structure effectively leverages heterojunction-induced depletion layer extension to achieve high sensitivity, rapid response and recovery to low hydrogen concentrations. Adjusting SnO_2 thickness is critical to balancing sensitivity and recovery time, with the Pd/SnO_2/WO_3/AAO sensor outperforming Pd/WO_3/AAO and Pd/SnO_2/AAO double-layer sensors in terms of detection limit, selectivity, and operational stability at

moderate temperatures. The response to 3% H_2 of optimized Pd/SnO_2/WO_3/AAO triple-layer thin film hydrogen sensor (Pd/SnO_2(56 nm)/WO_3/AAO) is 19.25% which is approximate twice that of Pd/WO_3/AAO sensor, at the same time, the response time (t_{rs90}) and recovery time (t_{rec90}) of Pd/SnO_2(56 nm)/WO_3/AAO are 95 s and 590 s respectively, especially, the recovery time is much shorter than Pd/SnO_2/AAO sensor. This work demonstrates a promising route to developing hydrogen sensing performance for SMOs hydrogen sensors for diverse industrial and environmental monitoring applications.

Acknowledgments

This work was supported by the Science and Technology Program of State Grid Anhui Electric Power Co., Ltd., (No. B31205230021).

Author contributions

Yu Zhang: Conceptualization, Methodology, Formal analysis, Investigation, Data curation, Writing - original draft.

Simin Wu: Methodology, Formal analysis.

Duoer Tang: Formal analysis, Writing - review & editing, Investigation.

Yao Wang: Validation, Investigation.

Junye Zhang: Methodology, Formal analysis, Validation.

Hongchuan Jiang: Writing - review & editing, Supervision, Funding acquisition, Project administration.

Xiaohui Zhao: Project administration, Resources, Writing - review & editing.

Xinwu Deng: Methodology, Project administration, Resources.

Data availability

Not applicable.

Conflict of interest

The authors declare that they have no known competing financial interests or personal relationships that could have appeared to influence the work reported in this paper.

Ethical approval

Not applicable.

Reference

[1] Z. Zhang, C. Yin, L. Yang, W. Jia, J. Zhou, H. Xu, D. Cao, Ceram. Int. **43**, 6693-99 (2017) https://doi.org/10.1016/j.ceramint.2017.02.065

[2] J. Tian, H. Jiang, X. Deng, L. Zhang, J. Zhang, X. Zhao, W. Zhang, Int. J. Hydrogen Energy **45**, 14594-601 (2020) https://doi.org/10.1016/j.ijhydene.2020.03.185

[3] N. Hacking, P. Pearson, M. Eames, Int. J. Hydrogen Energy **44**, 29805-48 (2019) https://doi.org/10.1016/j.ijhydene.2019.09.137

[4] Z. Li, S. Yan, Z. Wu, H. Li, J. Wang, W. Shen, Z. Wang, Y. Fu, Int. J. Hydrogen Energy **43**, 22746-57 (2018) https://doi.org/10.1016/j.ijhydene.2018.10.101

[5] Y. Dai, H. Jiang, X. Zhao, J. Tian, X. Deng, W. Zhang, J. Mater. Sci. Mater. Electron. **34**, 833 (2023) https://doi.org/10.1007/s10854-023-10219-x

[6] M. Kandyla, C.K. Chatzimanolis-Moustakas, E.P. Koumoulos, C. Charitidis, M. Kompitsas, Mater. Res. Bull. **49**, 552-59 (2017) https://doi.org/10.1016/j.materresbull.2013.09.044

[7] A. Kumar, A. Sanger, A. Kumar, R. Chandra, RSC Adv. **7**, 39666-75 (2017) https://doi.org/10.1039/c7ra05341j

[8] H.G. Girma, K.Y. Ryu, X. Tang, G.S. Ryu, R. Wang, Y. Kim, J.O. Choi, H.M. Lee, S. Jeon, S.H. Jung, J.M. Park, Y.J. Jung, J.Y. Kim, D.H. Hwang, Y.Y. Noh, B. Lim, H. Kong, S.H. Kim, ACS Sens. **8**, 3004-13 (2023) https://doi.org/10.1021/acssensors.3c00469

[9] N. Joshi, T. Hayasaka, Y. Liu, H. Liu, O. N. Oliveira Jr, L. Lin, Microchim. Acta **185**, 213 (2018) https://doi.org/10.1007/s00604-018-2750-5

[10] I.H. Kadhim, H.A. Hassan, J. Mater. Sci. Mater. Electron. **27**, 4356-62 (2016) https://doi.org/10.1007/s10854-016-4304-0

[11] Z. Li, G. Zhang, W. Gao, R. Zhao, Y. Wang, J. Mater. Sci. Mater. Electron. **30**, 18969-69 (2019) https://doi.org/10.1007/s10854-019-02253-5

[12] L. Chen, X. He, Y. Liang, Y. Sun, Z. Zhao, J. Hu, J. Mater. Sci. Mater. Electron. **27**, 11331-38 (2016) https://doi.org/10.1007/s10854-016-5257-z

[13] R.B. T, P.V. Karthik Yadav, A. Mondal, B. Ajitha , J. Jarugala, Y.A.K. Reddy, Int. J. Hydrogen Energy **50**, 878-88 (2024) https://doi.org/10.1016/j.ijhydene.2023.07.218

[14] W. Yu, Z. Shen, F. Peng, Y. Lu, M. Ge, X. Fu, Y. Sun, X. Chen, N. Dai, RSC Adv. **9**, 7723-28 (2019)

https://doi.org/10.1039/C9RA00116F
[15] A. Katoch, J. Kim, Y. Kwon, H.W. Kim, S.S. Kim, ACS Appl. Mater. Interfaces **7**, 11351-58 (2015) https://doi.org/10.1021/acsami.5b01817
[16] J. Zhang, L. Zhang, D. Leng, F. Ma, Z. Zhang, Y. Zhang, W. Wang, Q. Liang, J. Gao, H. Lu, Sens. Actuator B Chem. **306**, (2020) https://doi.org/10.1016/j.snb.2019.127575
[17] V.K. Tomer, K. Singh, H. Kaur, M. Shorie, P. Sabherwal, Sens. Actuator B Chem. **253**, 703-13 (2017) https://doi.org/10.1016/j.snb.2017.06.179
[18] K. Hu, Q. Zhao, Y. Guo, J. Zhang, J. Bao, Y. Yang, T. He, Y. Su, ACS Appl. Nano Mater. **5**, 6232-40 (2022) https://doi.org/10.1021/acsanm.2c00272
[19] D. Feng, L. Du, X. Xing, C. Wang, J. Chen, Z. Zhu, Y. Tian, D. Yang, ACS Sens. **6**, 733-41 (2021) https://doi.org/10.1021/acssensors.0c01280
[20] D. Zappa, V. Galstyan, N. Kaur, H.M.M. Arachchige, O. Sisman, E. Comini, Anal. Chim. Acta **1039**, 1-23 (2018) https://doi.org/10.1016/j.aca.2018.09.020
[21] P.M. Bulemo, J. Mater. Sci. Mater. Electron. **34**, 982 (2023) https://doi.org/10.1007/s10854-023-10445-3
[22] Y. Zhang, C. Hang, H. Jiang, X. Zhao, X. Deng, L. Wang, F. Ma, Z. Xu, Sens. Actuator B Chem. **423**, 136843 (2025) https://doi.org/10.1016/j.snb.2024.136843
[23] B.J. Kim, J.S. Kim, Int. J. Hydrogen Energy **39**, 16500-05 (2014) https://doi.org/10.1016/j.ijhydene.2014.05.071
[24] V. Ambardekar, T. Bhowmick, P.P. Bandyopadhyay, Int. J. Hydrogen Energy **47**, 15120-31 (2022) https://doi.org/10.1016/j.ijhydene.2022.03.005
[25] Y. Zhu, H. Wang, J. Liu, M. Yin, L. Yu, J. Zhou, Y. Liu, F. Qiao, J. Alloys Compd. **782**, 789-95 (2019) https://doi.org/10.1016/j.jallcom.2018.12.178
[26] N. Yamazoe, Sens. Actuator B Chem. **5**, 7-19 (1991) https://doi.org/10.1016/0925-4005(91)80213-4
[27] M.G. Kozodaev, R.I. Romanov, A.G. Chernikova, A.M. Markeev, J. Mater. Chem. C **125**, 21663-69 (2021) https://doi.org/10.1021/acs.jpcc.1c06149
[28] M. Yin, Y. Yao, H. Fan, S. Liu, J. Alloys Compd. **736**, 322-31 (2018) https://doi.org/10.1016/j.jallcom.2017.11.185
[29] D. Ramírez-Ortega, D. Guerrero-Araque, P. Acevedo-Peña, L. Lartundo-Rojas, R. Zanella, J. Mater. Sci. **55**, 16641-58 (2020) https://doi.org/10.1007/s10853-020-05188-z
[30] W. Ben Soltan, M. Abdalla, K. Harrath, J. Peng, Y. Zhang, Z. Cao, H. Liu, J. Chem. Chem. Eng. **11**, (2023) https://doi.org/10.1016/j.jece.2023.110637
[31] M. Sener, O. Sisman, N. Kilinc, Catalysts **13**, (2023) https://doi.org/10.3390/catal13030459
[32] X. Yin, W. Zhou, J. Li, Q. Wang, F. Wu, D. Dastan, D. Wang, H. Garmestani, X. Wang, S. Talu, J. Alloys Compd. **805**, 229-36 (2019) https://doi.org/10.1016/j.jallcom.2019.07.081
[33] W.T. Koo, H.J. Cho, D.H. Kim, Y.H. Kim, H. Shin, R.M. Penner, I.D. Kim, ACS Nano **14**, 13284-4322 (2020) https://doi.org/10.1021/acsnano.0c05307
[34] Q. Li, L. Wang, A. Xiao, L. Zhu, Z. Yang, Int. J. Hydrogen Energy **136**, 1282-305 (2025) https://doi.org/10.1016/j.ijhydene.2024.01.001

Supplementary Files

This is a list of supplementary files associated with this preprint. Click to download.

- SupplementaryMaterials.docx